Journal of Materials Chemistry C

ROYAL SOCIETY OF CHEMISTRY

PAPER

View Article Online
View Journal | View Issue

Cite this: J. Mater. Chem. C, 2023, 11, 11552

Crystalline-to-semicrystalline transition in lanthanide trifluoroacetates: implications for optical pressure and temperature sensing†

Regina G. Szlag and Federico A. Rabuffetti *

We report the serendipitous discovery of a pressure-dependent, crystalline-to-semicrystalline, reversible transition in the solid solution $Eu_{1-x}Tb_x(tfa)_3(H_2O)_3$ (tfa = CF_3COO). This transition is observed across the entire composition range upon reducing pressure from atmospheric to sub-100 mTorr levels. In the case of mixed-metal trifluoroacetates, switching from the atmospheric to the low-pressure phase leads to a drastic reduction in the intensity of green emission from Tb^{3+} and enhanced red emission from Eu^{3+}. The low-pressure phase shows not only enhanced Tb-to-Eu energy transfer but also a multisite distribution of lanthanide emitters. The crystalline-to-semicrystalline transition results from a disruption of hydrogen bonds and van der Waals interactions responsible for the long-range order observed in the atmospheric phase, likely driven by chemical changes such as vacuum-induced removal of terminal acuo ligands. The distinct luminescence responses of the atmospheric and low-pressure phases of $Eu_{1-x}Tb_x(tfa)_3(H_2O)_3$ have direct implications for the potential of mixed-metal trifluoroacetates as optical sensors. On the one hand, this contrast could be exploited to realize a two-state luminescent pressure sensor, though with the limitations imposed by the kinetics of the pressure-dependent transition, which takes about a day to complete in either direction under the experimental conditions observed in this work. On the other hand, the much weaker intensity of the emission from Tb^{3+} relative to that of Eu^{3+} in the low-pressure phase (≈2 orders of magnitude) limits the robustness of the red-to-green ratio as a thermometric parameter for luminescent thermometry.

Received 2nd June 2023,
Accepted 2nd August 2023

DOI: 10.1039/d3tc01924a

rsc.li/materials-c

Introduction

Lanthanide trifluoroacetates of formula $Ln(tfa)_3(H_2O)_3$ (Ln = rare-earth, Y; tfa = CF_3COO) were first reported by Roberts in 1961.[1] Since then, they have been extensively used as precursors in the synthesis of fluoride,[2–7] oxyfluoride,[3,8,9] and oxide[10–13] materials and nanomaterials. Their reactivity in the solid-state and in solution is thus well-established. By contrast, when it comes to their light-emitting properties, only a handful of studies have been reported.[14–21] These reports probed the room-temperature photoluminescence of $Ln(tfa)_3(H_2O)_3$ as a means of elucidating structural details[14,16–18] or of understanding the impact of organic sensitizers on lanthanide emission.[15,19–21] The temperature dependence of the luminescence response of these materials has not been studied. This is remarkable considering the widespread interest in identifying hybrid organic–inorganic platforms amenable to the design of lanthanide-based luminescent thermometers. Molecular complexes of varying nuclearity,[22–24] coordination polymers,[25,26] and metal–organic frameworks[25,27–29] are among the hybrid materials that have been explored as hosts for lanthanide emitters. Special emphasis has been placed on bimetallic systems featuring Eu^{3+} and Tb^{3+}. This lanthanide pair exhibits temperature-dependent energy transfer[23,30,31] from green emitting Tb^{3+} (donor) to red emitting Eu^{3+} (acceptor), a feature that has been extensively exploited to create thermometers in which the ratio between red and green emissions serves as the thermometric parameter.[22–29] To the best of our knowledge, however, this strategy has not been explored using mixed-metal trifluoroacetates of formula $(Eu,Tb)(tfa)_3(H_2O)_3$.

Lanthanide trifluoroacetates exhibit a number of crystal-chemical features that are interesting from the standpoint of optical sensing. The $Ln(tfa)_3(H_2O)_3$ isostructural series encompasses almost all rare-earths,[32] with crystal structures of Pr^{3+}, Nd^{3+}, Eu^{3+}, Gd^{3+}, Tb^{3+}, Dy^{3+}, Tm^{3+}, and Lu^{3+} trifluoroacetates available in the Cambridge Structural Database (CCDC No. 1151211, 1046357, 1865213, 280700, 188896, 137847, 1166544, and 1296232, respectively). The crystal structure of $Ln(tfa)_3(H_2O)_3$

Department of Chemistry, Wayne State University, Detroit, MI 48202, USA. E-mail: far@chem.wayne.edu

† Electronic supplementary information (ESI) available: (1) Additional results from Rietveld analyses, and (2) additional results from luminescence studies. See DOI: https://doi.org/10.1039/d3tc01924a

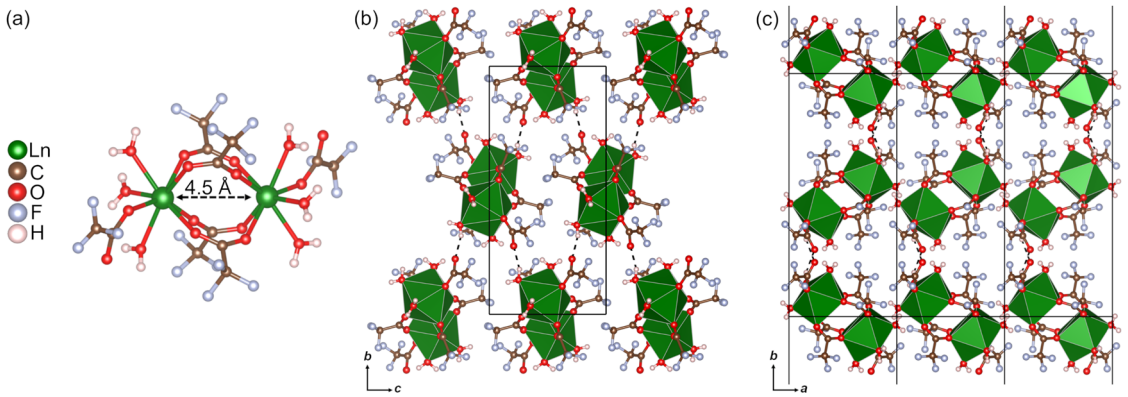

Fig. 1 Crystal structure of $Ln(tfa)_3(H_2O)_3$. (a) Ball-and-stick view of $Ln_2(tfa)_6(H_2O)_6$ dimers. (b) Polyhedral view of a single layer projected along [100] and extending in the *bc* plane. Layers result from connecting neighboring dimers with hydrogen bonds (depicted with black dashed lines). (c) View of the structure projected along [100] showing three layers stacked along the *a* axis. Unit cells are depicted with solid lines.

is shown Fig. 1. It crystallizes in the monoclinic $P2_1/c$ space-group and the building block consists of centrosymmetric dimers of formula $Ln_2(tfa)_6(H_2O)_6$ (Fig. 1(a)). The lanthanide metal occupies a site with C_1 symmetry and is eight-coordinated by five oxygen atoms belonging to five trifluoroacetato groups and three oxygen atoms from terminal acuo ligands. The coordination geometry is distorted square antiprismatic. Ln–O bond distances range from 2.34 to 2.47 Å for Eu^{3+} and from 2.32 to 2.45 Å for Tb^{3+}. Lanthanide atoms in $Ln_2(tfa)_6(H_2O)_6$ dimers are connected by four carboxylato bridges and sit ≈4.5 Å apart. Each dimer is connected to four neighboring dimers through hydrogen bonds involving trifluoroacetato ligands as acceptors and acuo ligands as donors. This connectivity leads to the formation of layers that extend in the *bc* plane (Fig. 1(b)). The shortest distance between lanthanide atoms in neighboring dimers within a layer is ≈8.3 Å. The three-dimensional structure of $Ln(tfa)_3(H_2O)_3$ results from stacking these layers along the *a* axis (Fig. 1(c)). Layers are held together by van der Waals interactions, a feature that is not uncommon in layered trifluoroacetates.[33] The shortest distance between lanthanide atoms belonging to dimers in adjacent layers is ≈6.2 Å. Two structural features of $Ln(tfa)_3(H_2O)_3$ that are noteworthy in the context of this work are (i) the significance of hydrogen bonds and van der Waals interactions for the stability of the observed structural motif, and (ii) the presence of Ln–Ln distances below 10 Å. The sensitivity of hydrogen bonds and van der Waals interactions to physicochemical parameters such as pressure and temperature[34] provides firm chemical and structural bases to explore the potential of $Ln(tfa)_3(H_2O)_3$ as a sensor for these external stimuli. Likewise, short intermetallic distances are expected to facilitate energy transfer between Tb^{3+} and Eu^{3+}, thereby supporting the sensitivity of the luminescence response towards external stimuli, particularly towards temperature. Finally, the fact that $Eu(tfa)_3(H_2O)_3$ and $Tb(tfa)_3(H_2O)_3$ are isostructural creates the opportunity to use the composition of the $Eu_{1-x}Tb_x(tfa)_3(H_2O)_3$ solid solution as a synthetic lever to tune sensing performance.

With these considerations in mind, our initial goal was to examine the luminescence response of $Eu_{1-x}Tb_x(tfa)_3(H_2O)_3$ as a function of the Eu/Tb ratio and identify the most suitable composition for optical temperature sensing. Early in the course of that study, which requires reduced pressures to achieve accurate temperature control below room temperature, we discovered that $Eu_{1-x}Tb_x(tfa)_3(H_2O)_3$ undergoes a pressure-dependent, crystalline-to-semicrystalline, reversible transition that significantly alters its emission spectrum. This unexpected observation led us to focus our efforts on understanding the kinetics, reversibility, and structural bases of the transition due to its potential implications for optical pressure sensing. This article is organized into three sections that reflect the order in which experiments were conducted. Section I is devoted to establishing the compositional dependence of the luminescence response of the $Eu_{1-x}Tb_x(tfa)_3(H_2O)_3$ solid solution. Polycrystalline trifluoroacetates are first interrogated with powder X-ray diffraction to probe their phase purity. Then, their room-temperature luminescence is screened using steady-state and time-resolved spectrofluorometry with the goal of selecting the most promising composition for variable-temperature and luminescence thermometry studies. The discovery of the pressure-dependent transition is presented in Section II. Luminescence and powder X-ray diffraction studies are carried out under variable pressure on selected members of the solid solution. These studies aim to characterize the low-pressure phase with regards to its light emitting properties and atomic structure, as well as the kinetics and reversibility of the atmospheric-to-low-pressure transition. Finally, the feasibility of using $Eu_{1-x}Tb_x(tfa)_3(H_2O)_3$ as an optical sensor for pressure and temperature is discussed in Section III using $Eu_{0.9}Tb_{0.1}(tfa)_3(H_2O)_3$ as a case study. Open questions and future directions to address these challenges are discussed.

Experimental

Synthesis of $Eu_{1-x}Tb_x(tfa)_3(H_2O)_3$

All experiments were carried out under nitrogen atmosphere using standard Schlenk techniques. Eu_2O_3 (99.9%), Tb_2O_3 (99.99%), and anhydrous CF_3COOH (99%) were purchased

from Sigma-Aldrich and used without further purification. Double-distilled water was employed as a cosolvent. $Eu_{1-x}Tb_x(tfa)_3(H_2O)_3$ (x = 0, 0.1, 0.2, 0.5, 0.8, 0.9, 1) polycrystalline solids were obtained *via* solvent evaporation.[35,36] Stoichiometric amounts of Eu_2O_3 and Tb_2O_3 were added to a 50 mL two-neck round-bottom flask containing 1.5 mL of tfaH and 1.5 mL of double distilled water; the total metal content was 1 mmol. While stirring, the solution was heated at 65 °C for 12 h under air to obtain a colorless transparent solution. The flask containing the reaction mixture was immersed in a sand bath and solvent evaporation took place at 65 °C for 18 h under a constant flow of dry nitrogen ($\approx$100 mL min^{-1}). White solids were obtained and stored under static nitrogen atmosphere.

Powder X-ray diffraction (PXRD)

PXRD patterns of $Eu_{1-x}Tb_x(tfa)_3(H_2O)_3$ were collected using a Bruker D2 Phaser diffractometer operated at 30 kV and 10 mA. Cu Kα radiation (λ = 1.5418 Å) was employed. A nickel filter was used to remove Cu Kβ radiation. Patterns were collected in the 8–70° 2θ range using a step size of 0.0125° and a step time of 0.5 s. The pressure-dependent transition of $Eu_{1-x}Tb_x(tfa)_3(H_2O)_3$ was studied using a Bruker D8 DaVinci powder diffractometer paired with an Anton Paar TTK 450 cryostat, which allowed data collection under atmospheric pressure and under vacuum. Vacuum levels in the cryostat were monitored by a convection-enhanced Pirani gauge (Kurt J. Lesker Model No. KJL275807LL). The diffractometer was operated at 40 kV and 40 mA. Cu Kα radiation was employed. Diffractograms were collected in the 8–48° 2θ range using a step size of 0.010° and a step time of 1.2 s. All diffractograms were recorded at room temperature.

Rietveld analysis

Rietveld analyses[37,38] of PXRD patterns were carried out using the General Structure Analysis System (GSAS) with the graphical user interphase (EXPGUI).[39,40] The following parameters were refined: (1) scale factor; (2) background, which was modeled using a shifted Chebyschev polynomial function; (3) peak shape, which was modeled using a modified Thompson–Cox–Hasting pseudo-Voight function;[41] (4) lattice constants; (5) atomic coordinates of the lanthanide atoms; (6) atomic coordinates of the trifluoroacetato ligands, with each ligand considered as a rigid body; (7) an isotropic displacement parameter for lanthanide atoms; and (8) an isotropic displacement parameter for all H, C, O, and F atoms belonging to trifluoroacetato and acuo ligands. Atomic coordinates of the acuo ligands were not refined. Metal site occupation factors were fixed at their nominal values. Difference curves and R_{wp} residuals were employed to assess the quality of the refined structural models. Crystal structures were visualized using VESTA.[42]

Spectrofluorometry

Luminescence analyses of $Eu_{1-x}Tb_x(tfa)_3(H_2O)_3$ were conducted using a Horiba Fluorolog 3–222. Excitation and emission spectra were collected using a 450 W xenon lamp as the continuous wave excitation source and a photomultiplier tube R928 as the detector. Luminescence decays were recorded using a 370 nm Horiba SpectraLED as the pulsed excitation source. The pressure-dependent transition of $Eu_{1-x}Tb_x(tfa)_3(H_2O)_3$ was studied by loading samples into a Lake Shore Cryotronics VPF-800 cryostat. The cryostat was equipped with a custom-made sample holder consisting of a copper block with a 12 mm diameter by 0.8 mm deep sample cavity. Powder samples were held in place by a fluorescence-free UV grade fused silica window secured by a stainless steel retainer and four spring-loaded screws. Spectra and decays were then collected under dynamic vacuum as monitored by a convection-enhanced Pirani gauge (Kurt J. Lesker Model No. KJL275807LL). The same experimental setup was used to probe temperature-dependent luminescence between 100 and 300 K. A Lake Shore Cryotronics 335–3060 controller and a thermocouple directly connected to the copper holder provided temperature readings with a ±0.2 K accuracy. Slit widths for data collection ranged from 0.7 to 1.2 nm. All spectra were corrected for lamp power fluctuations and detector sensitivity.

Results and discussion

Section I. Composition-dependent luminescence response of $Eu_{1-x}Tb_x(tfa)_3(H_2O)_3$

The chemical purity of polycrystalline $Eu_{1-x}Tb_x(tfa)_3(H_2O)_3$ was probed prior to examining luminescence response. Rietveld analysis of PXRD data was carried out to this end. Results from these studies are summarized in Fig. 2. Refinement of the previously reported $Ln(tfa)_3(H_2O)_3$ structure (*vide supra*) provides a good fit to the experimental patterns of all members of the $Eu_{1-x}Tb_x(tfa)_3(H_2O)_3$ series. Taking $Eu_{0.9}Tb_{0.1}(tfa)_3(H_2O)_3$ as a representative example, all diffraction maxima are indexed to the mixed-metal trifluoroacetate, demonstrating the phase purity of the solid (Fig. 2(a)). Refined structural parameters for this and other compositions are given in the ESI† along with the corresponding Rietveld plots (Fig. S1 and Tables S1–S8, ESI†). Unit cell constants decrease upon increasing the concentration of terbium (Fig. 2(b)), as expected on the basis of the ionic radii of eight-coordinated Eu^{3+} (1.07 Å) and Tb^{3+} (1.04 Å).[43] The volume of the unit cell decreases linearly with terbium concentration, indicating the formation of a solid solution between $Eu(tfa)_3(H_2O)_3$ and $Tb(tfa)_3(H_2O)_3$ over the entire concentration range.

The luminescence response of $Eu_{1-x}Tb_x(tfa)_3(H_2O)_3$ was screened at room temperature with the aim of identifying the most suitable compositions for variable-temperature luminescence studies. Steady-state excitation and emission spectra were collected for all members of the solid solution. Representative spectra are shown in Fig. 3 for $Eu_{0.9}Tb_{0.1}(tfa)_3(H_2O)_3$; spectra for other compositions are given in the ESI† (Fig. S2 and S3). Excitation spectra were collected monitoring emissions of Eu^{3+} and Tb^{3+} at 612 ($^5D_0 \rightarrow {}^7F_2$) and 544 nm ($^5D_4 \rightarrow {}^7F_5$), respectively. Spectra are dominated by metal-centered f–f excitations $^7F_0 \rightarrow {}^5L_6$ (393 nm) and $^7F_6 \rightarrow {}^5L_{10}$ (369 nm) of Eu^{3+} and

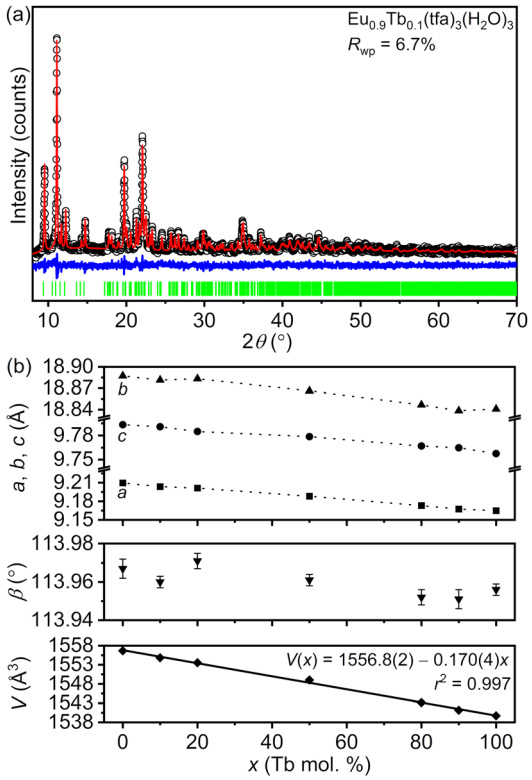

Fig. 2 (a) Rietveld analysis of the PXRD pattern of $Eu_{0.9}Tb_{0.1}(tfa)_3(H_2O)_3$. Experimental (○) and calculated patterns (—), difference curve (—, offset for clarity), and tick marks (|) corresponding to the calculated positions of the diffraction maxima are shown. (b) Unit cell constants (*a*, *b*, *c*, *β*) and volume (*V*) of $Eu_{1-x}Tb_x(tfa)_3(H_2O)_3$ as a function of the terbium concentration (*x*). Dotted lines are guides-to-the-eye. A linear fit of *V* as a function of *x* is shown as a solid line. Fit parameters and residual (r^2) are given.

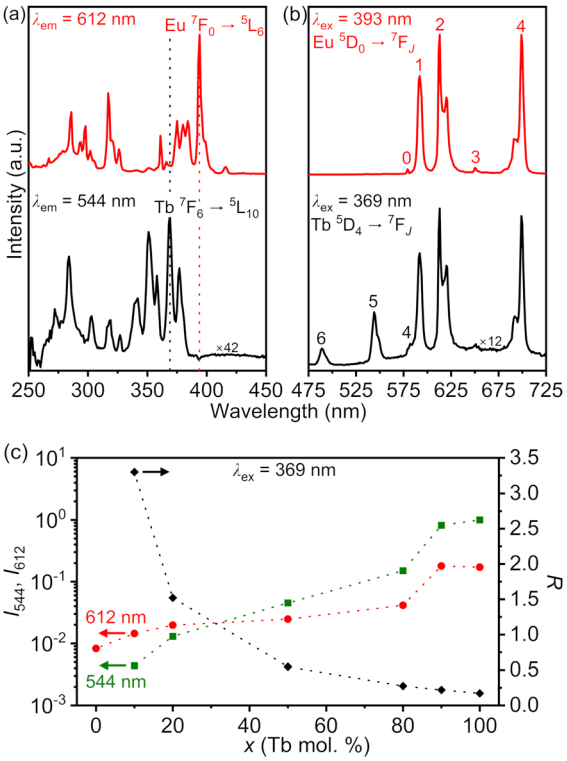

Fig. 3 Room-temperature excitation (a) and emission spectra (b) of $Eu_{0.9}Tb_{0.1}(tfa)_3(H_2O)_3$. Selected f–f transitions of Eu^{3+} and Tb^{3+} are labeled. (c) Integrated intensities of the emission bands centered at 544 and 612 nm (I_{544}, I_{612}) as a function of the terbium concentration in $Eu_{1-x}Tb_x(tfa)_3(H_2O)_3$. The red-to-green luminescence intensity ratio (*R*) is also plotted. Dotted lines are guides-to-the-eye.

Tb^{3+}, respectively (Fig. 3(a)). The emission spectrum collected under europium-centered excitation at 393 nm shows the usual emission bands arising from $^5D_0 \rightarrow {}^7F_J$ (J = 0–4) transitions of Eu^{3+} (Fig. 3(b)). On the other hand, terbium-centered excitation at 369 nm leads to emission from both Tb^{3+} and Eu^{3+}, indicating that Tb-to-Eu energy transfer takes place. Emission bands corresponding to the $^5D_4 \rightarrow {}^7F_J$ (J = 6–4) transitions of Tb^{3+} are observed at 488, 544, and 583 nm; the $^5D_4 \rightarrow {}^7F_3$ emission is centered at 621 nm and overlaps with the red emission band of Eu^{3+} at 612 nm. The occurrence of Tb-to-Eu energy transfer was confirmed by monitoring emission upon excitation of the $^7F_6 \rightarrow {}^5D_4$ terbium-centered transition at 488 nm (see ESI,† Fig. S4). No Tb^{3+} emission bands were observed upon excitation of the $^7F_0 \rightarrow {}^5D_2$ transition of Eu^{3+} at 464 nm, suggesting that Eu-to-Tb energy transfer does not take place (see ESI,† Fig. S4). Green and red emission bands observed under 369 nm excitation were integrated in the 525–569 and 604–637 nm ranges, respectively, to extract the corresponding integrated intensities I_{544} and I_{612} and compute the red-to-green luminescence intensity ratio (R, eqn (1)). This ratio is

$$R = \frac{I_{612}}{I_{544}} \quad (1)$$

typically used as the thermometric parameter in luminescence thermometry studies of systems containing Eu^{3+} and Tb^{3+}. I_{544} and I_{612} increase with terbium concentration and R reaches a maximum value of 3.3 for $Eu_{0.9}Tb_{0.1}(tfa)_3(H_2O)_3$ (Fig. 3(c)). For this particular composition R drops to 1.6 at 77 K (see ESI,† Fig. S5), in line with previous reports that showed that the observed Tb-to-Eu energy transfer is thermally activated.

Time-resolved radiative decays of Tb^{3+} donors were collected with the goal of estimating Tb-to-Eu energy transfer efficiency and further narrowing the scope of compositions for variable-temperature luminescence studies. Decays were excited at 370 nm and monitored at 544 nm (Tb^{3+} $^5D_4 \rightarrow {}^7F_5$). Results from these studies are summarized in Fig. 4. The room-temperature luminescence decay of $Eu_{0.9}Tb_{0.1}(tfa)_3(H_2O)_3$ is discussed herein as a representative example; decays of other members of the $Eu_{1-x}Tb_x(tfa)_3(H_2O)_3$ solid solution are given in the ESI† (Fig. S6). The decay of the $^5D_4 \rightarrow {}^7F_5$ emission of Tb^{3+} is well fit by a monoexponential function with lifetime τ = 677 μs (Fig. 4(a)). Lifetime is minimum for $Eu_{0.9}Tb_{0.1}(tfa)_3(H_2O)_3$, which has the highest concentration of Eu^{3+} acceptors. Increasing the terbium concentration in the solid solution leads to an increase in lifetime, which reaches a maximum of 1134 μs in $Tb(tfa)_3(H_2O)_3$ (Fig. 4(b)). Lifetimes were used to estimate Tb-to-Eu energy transfer efficiencies (η_{ET}, eqn (2)) and rate constants (k_{ET}, eqn (3)); here,

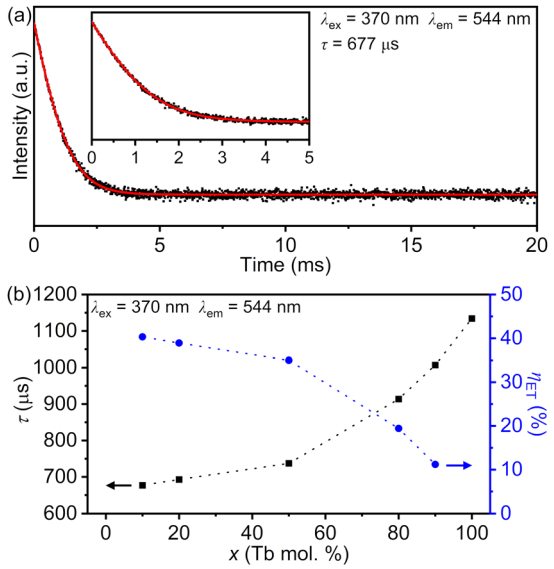

Fig. 4 (a) Room-temperature luminescence decay of $Eu_{0.9}Tb_{0.1}(tfa)_3(H_2O)_3$ excited at 370 nm and monitored at 544 nm (Tb^{3+} $^5D_4 \rightarrow {}^7F_5$). The decay is shown in logarithmic scale and the corresponding monoexponential fit is depicted as a solid red line. A magnified view between 0 and 5 ms is shown in the inset. (b) Lifetime (τ) and Tb-to-Eu energy transfer efficiency (η_{ET}) as a function of the terbium concentration in $Eu_{1-x}Tb_x(tfa)_3(H_2O)_3$. Dotted lines are guides-to-the-eye.

τ(Eu,Tb) and τ(Tb) are the lifetimes of the mixed-metal and terbium

$$\eta_{ET} = 1 - \frac{\tau(Eu,Tb)}{\tau(Tb)} \quad (2)$$

$$k_{ET} = \frac{1}{\tau(Eu,Tb)} - \frac{1}{\tau(Tb)} \quad (3)$$

trifluoroacetates, respectively. Energy transfer efficiency is maximum for $Eu_{0.9}Tb_{0.1}(tfa)_3(H_2O)_3$ with a value of 40.3% (k_{ET} = 595 s^{-1}) and decreases with terbium concentration until reaching a minimum of 11.2% for $Eu_{0.1}Tb_{0.9}(tfa)_3(H_2O)_3$ (k_{ET} = 111 s^{-1}).

Section II. Pressure-dependent crystalline-to-semicrystalline transition of $Eu_{1-x}Tb_x(tfa)_3(H_2O)_3$

Results from steady-state and time-resolved spectrofluorometric studies led us to choose $Eu_{0.9}Tb_{0.1}(tfa)_3(H_2O)_3$ as the composition to probe variable-temperature luminescence and evaluate its potential as an optical thermometer. With this goal in mind, polycrystalline $Eu_{0.9}Tb_{0.1}(tfa)_3(H_2O)_3$ was loaded into our cryostat and vacuum was pulled with the goal of degassing the system prior to variable-temperature experiments. Establishing a degassing procedure typically involves optimizing degassing temperature and time to ensure repeatable luminescence response without compromising the chemical and structural integrity of the material. In the course of this optimization process we observed that the emission spectrum of $Eu_{0.9}Tb_{0.1}(tfa)_3(H_2O)_3$ excited at 369 nm changed upon pulling vacuum at room temperature, revealing a pressure-dependent transition with the potential to serve for optical pressure sensing. We decided to conduct a detailed investigation of this transition, particularly regarding its kinetics and reversibility. To this end, the sample was first subject to dynamic vacuum and emission was monitored as a function of time and pressure. Then, vacuum was released, the sample exposed to air (atmospheric pressure, 760 Torr, relative humidity 23–27%), and emission monitored as a function of time. Results from this study are summarized in Fig. 5. All emission spectra shown therein were collected under 369 nm excitation using the same conditions. Qualitative inspection of the spectra reveals the following features of the pressure-dependent transition of $Eu_{0.9}Tb_{0.1}(tfa)_3(H_2O)_3$: (i) a drastic reduction in the intensity of the emission bands arising from Tb^{3+} (488 and 544 nm) and a concomitant increase in the intensity of the emission bands from Eu^{3+} upon decreasing pressure, indicating a change in the Tb-to-Eu energy transfer mechanism and/or efficiency; (ii) a change in the Stark splitting of the hypersensitive $^5D_0 \rightarrow {}^7F_2$ transition of Eu^{3+}, reflecting that the local atomic environment of Eu^{3+} ions in the low-pressure phase is different from that in the atmospheric phase; (iii) the most pronounced spectral changes occur within the first few hours under vacuum levels below 100 mTorr ($\approx$8 h), indicating the that the bulk of the atmospheric-to-low-pressure phase conversion occurs within that time window; and (iv) the atmospheric phase is recovered after 24 h of exposure to air, pointing to the reversibility of the transition. The evolution of the integrated intensities of the emission bands centered at 544 (Tb^{3+}) and 612 nm (Eu^{3+}) with time and pressure provides quantitative support to the above-mentioned conclusions. I_{544} and I_{612} were extracted by integrating emission bands in the 535–559 and 603–638 nm ranges, respectively, and are plotted in Fig. 6. Inspection of this plot confirms that the bulk of the transition occurs in the first few hours under vacuum. After 8 h under reduced pressure (41–81 mTorr), the intensity of the green emission of Tb^{3+} has decreased $\approx$17 times relative to its value in the atmospheric phase, while the intensity of the red emission of Eu^{3+} has increased $\approx$2.8 times. Changes observed afterwards are comparatively minor; after 26 h under vacuum, these decrease and increase factors are $\approx$24 and 3.0, respectively. As a result, the red-to-green luminescence intensity ratio increases two orders of magnitude upon going from the atmospheric (R = 3.6) to the low-pressure phase (R = 266 at 26 mTorr). The evolution of integrated intensities with time and pressure also confirms the reversibility of the transition. Once vacuum is released and the sample is exposed to air for 24 h, I_{544} and I_{612} recover the values corresponding to the atmospheric phase. The pressure-dependent transition observed in $Eu_{0.9}Tb_{0.1}(tfa)_3(H_2O)_3$ deserves a few additional comments. This transition is also noticeable in the excitation spectra monitored at 544 and 612 nm (see ESI,† Fig. S7). Moreover, it is reproducible over multiple batches of $Eu_{0.9}Tb_{0.1}(tfa)_3(H_2O)_3$, although minor fluctuations are observed in the relative intensities of the Stark sublevels of the $^5D_0 \rightarrow {}^7F_2$ hypersensitive transition of Eu^{3+}. Finally, and most importantly, it is not exclusive to the mixed-metal trifluoroacetates since it is also observed in the end-members $Eu(tfa)_3(H_2O)_3$ and $Tb(tfa)_3(H_2O)_3$ (see ESI,† Fig. S8 and S9). In the case of $Tb(tfa)_3(H_2O)_3$, pressure reduction does

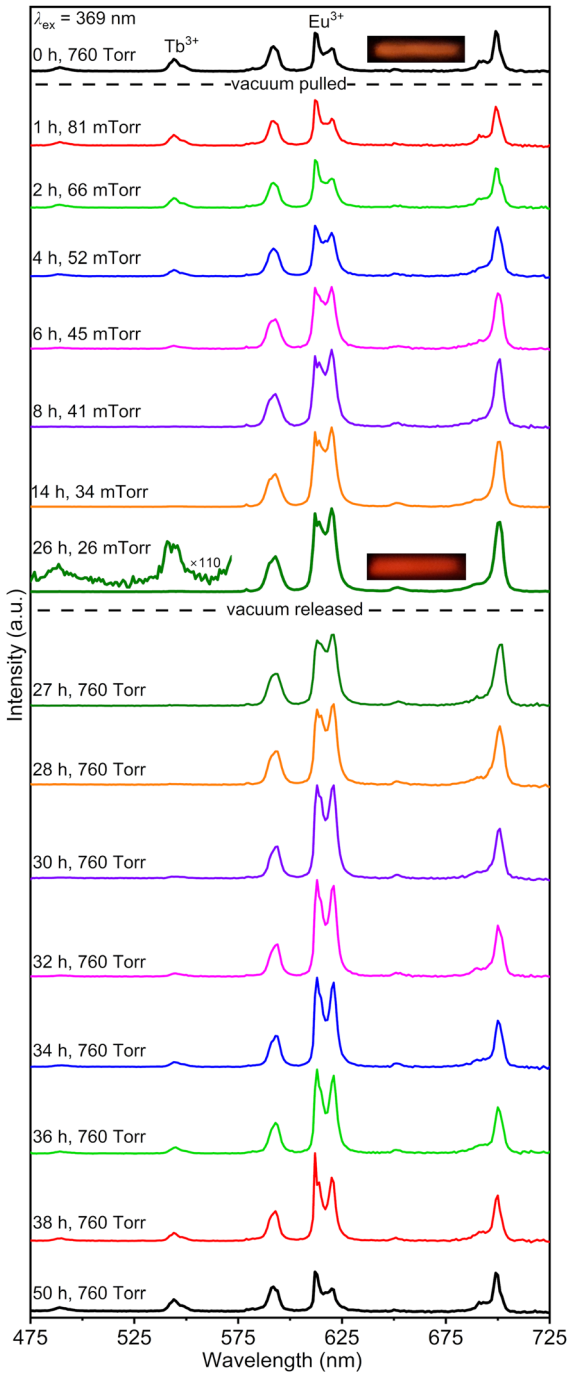

Fig. 5 Room-temperature emission spectra of $Eu_{0.9}Tb_{0.1}(tfa)_3(H_2O)_3$ at atmospheric pressure and under dynamic vacuum. Spectra are labeled with the time and pressure at which they were collected. Atmospheric-to-low-pressure and low-pressure-to-atmospheric transitions are observed upon pulling and releasing vacuum, respectively. Thicker lines are used to highlight the spectra of the atmospheric phase at 0 and 50 h and that of the low-pressure phase at 26 h. Digital pictures under 369 nm illumination are shown for both phases.

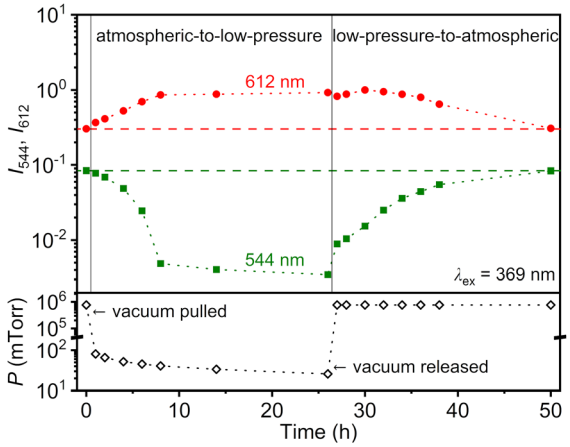

Fig. 6 Integrated intensities of the 544 and 612 nm emission bands (I_{544}, I_{612}) of $Eu_{0.9}Tb_{0.1}(tfa)_3(H_2O)_3$ at atmospheric pressure and under dynamic vacuum. Intensities are plotted as a function of experiment time. Dotted and dashed lines are guides-to-the-eye. Horizontal dashed lines highlight the fact that the atmospheric phase is restored 24 h after releasing vacuum.

not result in a major reduction of the intensity of the green emission band centered at 544 nm like it does in $Eu_{0.9}Tb_{0.1}(tfa)_3(H_2O)_3$, where Eu^{3+} acceptors are present. This observation confirms that Tb-to-Eu energy transfer in the low-pressure phase of $Eu_{0.9}Tb_{0.1}(tfa)_3(H_2O)_3$ occurs and is quite efficient (*vide infra*).

Time-resolved radiative decays were collected to shed further light into the pressure-dependent transition and into the luminescence response of the low-pressure phase of $Eu_{0.9}Tb_{0.1}(tfa)_3(H_2O)_3$. The sample was loaded into our cryostat and degassed under vacuum at 325 K (52 °C) for 12 h; thermal analysis showed no chemical changes occured upon heating to this temperature (see ESI,† Fig. S10). Once degassing was completed, decays were collected in the 100–300 K temperature range under dynamic vacuum (6.9–7.4 mTorr) by exciting at 370 nm and monitoring emission at 544 nm (Tb^{3+} $^5D_4 \rightarrow {}^7F_5$). Results from these studies are summarized in Fig. 7. Unlike the monoexponential decay in the atmospheric phase, Tb^{3+} decays in the low-pressure phase may be adequately fit with a triexponential function (Fig. 7(a)). Such function is given below (eqn (4)), where $I(t)$ is the experimental intensity at time t, A, A_1, A_2, and A_3 are constants, and τ_1, τ_2, and τ_3 are lifetimes. Percent contributions F_i are computed from these adjustable parameters (eqn (5)). The observation of a

$$I(t) = A + A_1 \exp\left(-\frac{t}{\tau_1}\right) + A_2 \exp\left(-\frac{t}{\tau_2}\right) + A_3 \exp\left(-\frac{t}{\tau_3}\right) \quad (4)$$

$$F_i = 100 \times \frac{A_i \tau_i}{\sum_i A_i \tau_i} \quad (5)$$

multiexponential decay points to a multisite distribution of lanthanide ions in the low-pressure phase, in line with the asymmetry of the 580 nm emission band arising from the $^5D_0 \rightarrow {}^7F_0$ transition of Eu^{3+} (see ESI,† Fig. S11). A change in the mechanism and/or dynamics of Tb-to-Eu energy transfer upon reducing pressure may also lead to a deviation from the monoexponential decay observed in the atmospheric phase. At 300 K, lifetimes equal 1003, 163, and 20 μs,

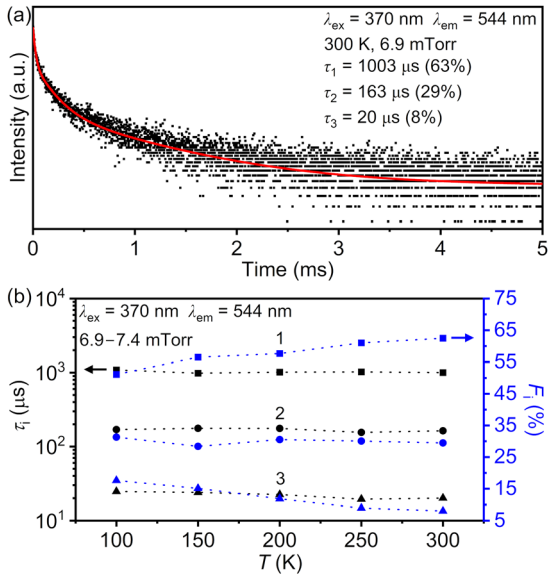

Fig. 7 (a) Luminescence decay of $Eu_{0.9}Tb_{0.1}(tfa)_3(H_2O)_3$ under dynamic vacuum at 300 K. Luminescence was excited at 370 nm and monitored at 544 nm (Tb^{3+} $^5D_4 \rightarrow {}^7F_5$). The decay is shown in logarithmic scale and the corresponding triexponential fit is depicted as a solid red line. Lifetimes (τ_1, τ_2, τ_3) and percent contributions (F_1, F_2, F_3) are given. (b) Lifetimes and percent contributions as a function of temperature. Dotted lines are guides-to-the-eye.

spanning three orders of magnitude and yielding an amplitude-weighted average lifetime ($\langle\tau\rangle$, eqn (6)) of 155 μs, significantly

$$\tau = \frac{\sum_i A_i \tau_i}{\sum_i A_i} \quad (6)$$

shorter than that observed for the atmospheric phase at room temperature (677 μs). Lifetimes and percent contributions extracted from triexponential fits are quite stable in the entire temperature range (Fig. 7(b)). τ_1, τ_2, and τ_3 oscillate within the 983–1087, 155–176, and 19–25 μs ranges, respectively. Likewise, F_1, F_2, and F_3 stay within the 51–63, 28–31, and 8–18% ranges, respectively. Experimental decays and fits at temperatures below 300 K are given in the ESI† (Fig. S12). Finally, we attempted to estimate the Tb-to-Eu average energy transfer efficiency in the low-pressure phase of $Eu_{0.9}Tb_{0.1}(tfa)_3(H_2O)_3$. To this end, we monitored the decay of the $^5D_4 \rightarrow {}^7F_5$ transition of Tb^{3+} in the low-pressure phase of the end-member $Tb(tfa)_3(H_2O)_3$ (*i.e.*, in the absence of Eu^{3+} acceptors, see ESI,† Fig. S13). Although a triexponential function was needed to correctly fit the decay at 100 K, both a biexponential and a triexponential function provided adequate fits at 300 K. Since parameters extracted from the latter were highly correlated, we chose to use a biexponential fit to model the experimental decay. Lifetimes of 1.96 (91%) and 7.19 ms (9%) were thus extracted, yielding an amplitude-weighted average lifetime $\langle\tau\rangle$ = 2.1 ms. This average lifetime is significantly longer than that observed in the mixed-metal $Eu_{0.9}Tb_{0.1}(tfa)_3(H_2O)_3$ at 300 K (155 μs) and provides further support to the high efficiency of Tb-to-Eu energy transfer in the low-pressure phase inferred on the basis of steady-state spectra. Average lifetimes in $Eu_{0.9}Tb_{0.1}(tfa)_3(H_2O)_3$ (155 μs) and $Tb(tfa)_3(H_2O)_3$ (2.1 ms) were used to estimate the average energy transfer efficiency,[44–46] yielding a value of 93% at 300 K (95% at 100 K). In summary, results from time-resolved luminescence studies point to a structural change leading to a multisite distribution of lanthanide ions and a nearly quantitative Tb-to-Eu energy transfer in the low-pressure phase of $Eu_{0.9}Tb_{0.1}(tfa)_3(H_2O)_3$.

With the luminescence data in hand, we set out to investigate the structural bases of the pressure-dependent transition using PXRD. Diffractograms of $Eu_{0.9}Tb_{0.1}(tfa)_3(H_2O)_3$ were sequentially collected under air (atmospheric pressure, 760 Torr, relative humidity 23–25%) and dynamic vacuum (14.4–22.3 mTorr) for a total of 5 air–vacuum cycles. In each cycle, the sample was exposed to air and vacuum for 24 h and 21 h, respectively, prior to data collection. All diffractograms were collected using the same conditions. This experiment took 11 days to complete and results are summarized in Fig. 8. An alternative view of the PXRD patterns of the atmospheric and low-pressure phases is given in the ESI† (see Fig. S14). Inspection of the patterns reveals the occurrence of a crystalline-to-semicrystalline transition. Patterns of the low-pressure phase consist of a few diffraction maxima of much lower intensity than those observed in the atmospheric phase. These maxima sit on a background typical of poorly crystalline materials. In other words, reduction of pressure causes a disruption of the long-range order in the atmospheric phase and leads to a significantly more disordered structure, in line with results from time-resolved luminescence experiments. Our efforts to elucidate the atomic arrangement of the low-pressure phase have been unsuccessful so far. Nonetheless, the crystal structure of the atmospheric phase provides a starting point to formulate a few hypotheses regarding this point. As mentioned earlier, three types of interactions may be distinguished in the atmospheric phase; these are (i) carboxylato bridges, which give rise to $Ln_2(tfa)_6(H_2O)_6$ dimers; (ii) hydrogen bonds, responsible for the long-range order of the dimers in layers; and (iii) van der Waals interactions that hold these layers together (*vide supra*, Fig. 1). We hypothesize that carboxylato bridges are the least affected by pressure reduction, whereas significant changes occur to lower energy interactions such as hydrogen bonds and van der Waals interactions. Hydrogen bonds in particular are highly susceptible to partial or total loss of terminal acuo ligands occurring upon reducing pressure (*i.e.*, dehydration). In other words, polynuclear clusters (*e.g.*, dimers) likely exist in the low-pressure phase and provide the local structural basis for Tb-to-Eu energy transfer, but their long-range arrangement in layers is disrupted. This disruption is undoubtedly reversible because PXRD data show that the atmospheric phase is recovered once vacuum is released and the sample exposed to air for 24 h, in agreement with luminescence data. The PXRD patterns of the atmospheric phase remain comparable over 5 air–vacuum cycles (Fig. 8, left panel), both in terms of number of maxima and relative intensities. A similar remark holds true for the patterns of the low-pressure phase (Fig. 8, right panel).

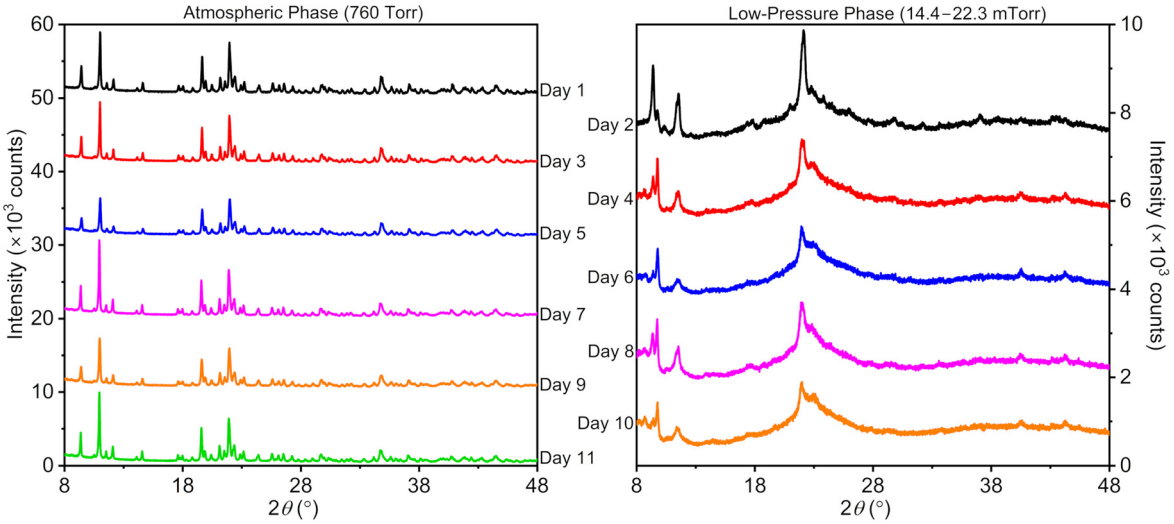

Fig. 8 PXRD patterns of $Eu_{0.9}Tb_{0.1}(tfa)_3(H_2O)_3$ collected over the course of 11 days in which the sample was subject to 5 air–vacuum cycles. In each cycle, the sample was exposed to air and dynamic vacuum for 24 and 21 h, respectively, prior to data collection. The sample surface was flattened on days 7 and 11 to get rid of the warping observed upon pressure reduction. Patterns of the crystalline atmospheric phase and of the semicrystalline low-pressure phase are shown in the left and right panels, respectively.

Section III. Pressure and temperature sensing using $Eu_{0.9}Tb_{0.1}(tfa)_3(H_2O)_3$

Pressure sensing. The pressure dependence of the transition of $Eu_{0.9}Tb_{0.1}(tfa)_3(H_2O)_3$ was further studied with an eye towards optical pressure sensing. We sought to probe whether this material could serve as a two-state or as a multistate sensor, *i.e.*, if it can be switched between the atmospheric and low-pressure phases only or if intermediate phases are also accessible. In addition, we aimed to establish pressure windows in which these phases are stable. With these goals in mind, $Eu_{0.9}Tb_{0.1}(tfa)_3(H_2O)_3$ was loaded into our cryostat and a flow needle valve was installed between the latter and the vacuum line. Coupled to the convection-enhanced Pirani gauge, this valve provided a straightforward way of adjusting the vacuum level in the cryostat. Starting from atmospheric pressure (760 Torr, needle valve closed), pressure was reduced stepwise by roughly an order of magnitude every 24 h until reaching a minimum (≈20 mTorr, needle valve fully open). In each step, emission spectra excited at 369 nm were collected at the beginning and at the end of the 24 h period, right before and after changing pressure. Relative humidity and ambient temperature fluctuated between 23 and 36% and 297 and 300 K, respectively. This experiment took 5 days to complete and results are summarized in Fig. 9, where the integrated intensities of the emission bands centered at 544 and 612 nm are plotted as a function of pressure. I_{544} and I_{612} were extracted by integrating bands in the 535–559 and 603–638 nm ranges, respectively; the corresponding spectra are given in the ESI† (Fig. S15). The atmospheric phase remains unchanged in the 760 × 10^3–677 mTorr pressure range. The onset of the transition is observed upon bringing pressure down to the 58.8–77.7 mTorr range. The intensity of the Tb^{3+} green emission at 544 nm decreases and that of the Eu^{3+} red emission at 612 nm

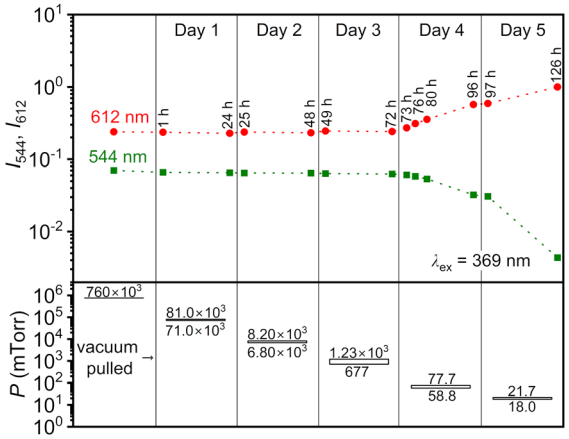

Fig. 9 Integrated intensities of the 544 and 612 nm emission bands (I_{544}, I_{612}) of $Eu_{0.9}Tb_{0.1}(tfa)_3(H_2O)_3$ at atmospheric pressure and under controlled dynamic vacuum. Intensities are labeled with the time at which the corresponding spectra were collected. Pressure windows for each day are depicted as box charts, with maximum and minimum pressure values shown above and below each box, respectively. Dotted lines are guides-to-the-eye.

increases as soon as this reduction of pressure occurs. Intensities do not stabilize within the following 24 h, despite pressure staying within a narrow window during that period. On this basis, we conclude that no intermediate phases with a stable luminescence response suitable for sensing are accessible under the experimental conditions observed in this work. It should also be mentioned that the mechanism by which pressure sensing is accomplished using $Eu_{0.9}Tb_{0.1}(tfa)_3(H_2O)_3$ is different from that of well-established optical pressure sensors, which are based on a continuous variation of the luminescence response with pressure (*i.e.*, emission line shift in Cr^{3+}-[47,48] and Sm^{2+}-activated[49] phosphors).

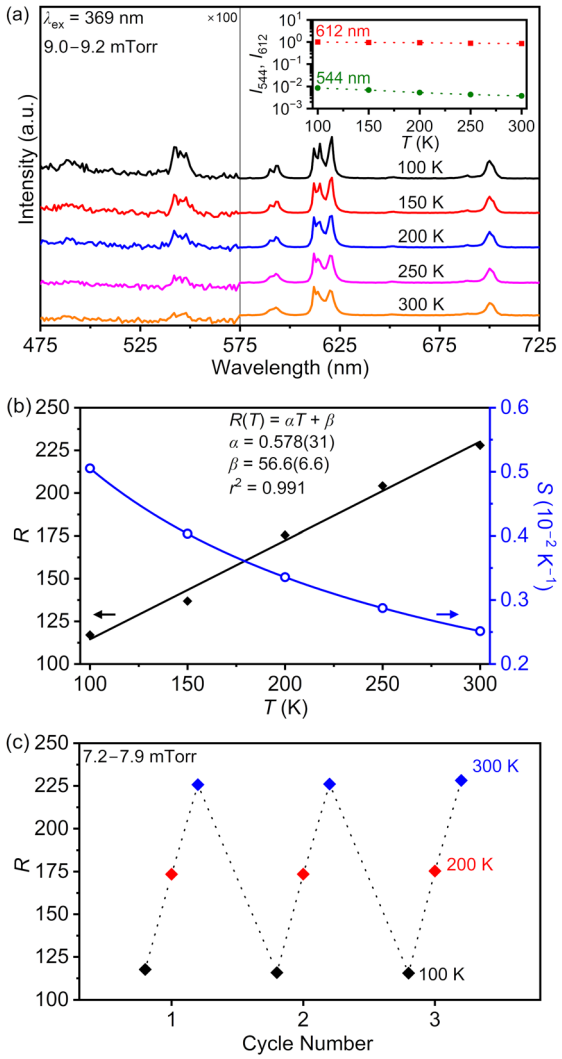

Fig. 10 (a) Variable-temperature emission spectra of $Eu_{0.9}Tb_{0.1}(tfa)_3(H_2O)_3$ under dynamic vacuum. The temperature-dependence of the integrated intensities of the 544 and 612 nm emission bands (I_{544}, I_{612}) is shown in the inset. (b) Luminescence intensity ratio (R) and thermometric sensitivity (S) as a function of temperature. A linear fit to experimental R values is depicted as a solid black line. Fit parameters and residual (r^2) are given. (c) Intensity ratio as a function of heating–cooling cycle number. Dotted lines are guides-to-the-eye.

Temperature sensing. Finally, we evaluated the feasibility of using the low-pressure phase of $Eu_{0.9}Tb_{0.1}(tfa)_3(H_2O)_3$ as a ratiometric thermometer. We undertook this task with the caveat that the very weak intensity of the Tb^{3+} emission band centered at 544 nm limits the robustness of the red-to-green luminescence intensity ratio R as a thermometric parameter. $Eu_{0.9}Tb_{0.1}(tfa)_3(H_2O)_3$ was loaded into our cryostat and degassed under vacuum at 325 K for 12 h. Then, emission spectra were collected in the 100–300 K temperature range under dynamic vacuum (9.0–9.2 mTorr). Spectra were recorded between 475 and 725 nm under 369 nm excitation. Emission bands centered at 544 and 612 nm were integrated between 535 and 559 nm and between 603 and 638 nm, respectively. Results from luminescence thermometry studies are summarized in Fig. 10. Inspection of the emission spectra shows the distinct temperature dependence of the bands centered at 544 and 612 nm (Fig. 10(a)). The integrated intensity of the former undergoes a larger drop than that of the latter, which remains practically constant throughout the entire temperature range. The fact that such drop is not observed in $Tb(tfa)_3(H_2O)_3$ (*i.e.*, in the absence of Eu^{3+} acceptors, see ESI,† Fig. S16) further supports that Tb-to-Eu energy transfer occurs in the low-pressure phase of $Eu_{0.9}Tb_{0.1}(tfa)_3(H_2O)_3$. The luminescent intensity ratio in this phase increases from 117 at 100 K to 227 at 300 K (Fig. 10(b)). The dependence of R on temperature may be adequately modeled with a linear function (eqn (7)) in

$$R(T) = \alpha T + \beta \quad (7)$$

which α and β are constants with values 0.578(31) and 56.6(6.6), respectively. A Mott–Seitz model with one nonradiative deactivation channel[50] and three adjustable parameters also fits $R(T)$; the resulting sigmoidal fit, however, provides little improvement over a linear fit (see ESI,† Fig. S17). Thus, the latter was used to estimate thermometric sensitivity (S, eqn (8)). Relative sensitivity values thus

$$S = \frac{1}{R(T)}\frac{dR(T)}{dT} \quad (8)$$

obtained range between 5×10^{-3} K^{-1} at 100 K and 2.5×10^{-3} K^{-1} at 300 K. These values are on the low end of sensitivity ranges reported for other lanthanide hybrids featuring Eu^{3+} and Tb^{3+}, particularly near room temperature.[22–29,51–53] Finally, repeatability, temperature accuracy, and resolution were assessed by subjecting $Eu_{0.9}Tb_{0.1}(tfa)_3(H_2O)_3$ to 3 heating–cooling cycles under dynamic vacuum (7.2–7.9 mTorr) and computing R values at 100, 200, and 300 K (Fig. 10(c)). Although values of the integrated intensities I_{612} and I_{544} showed some fluctuations (see ESI,† Fig. S18), R values remained remarkably consistent (115–118 at 100 K, 173–175 at 200 K, 226–228 at 300 K) yielding repeatabilities of 99%. These values and the thermometric scale given in eqn (7) were used to estimate calculated temperatures at 100, 200, and 300 K, yielding 103.3(2.1), 203.3(1.8), and 294.3(2.3) K, respectively (see ESI,† Table S9).

Conclusions

A pressure-dependent crystalline-to-semicrystalline transition was discovered in the $Eu_{1-x}Tb_x(tfa)_3(H_2O)_3$ solid solution. This transition occurs upon reducing pressure from atmospheric to sub-100 mTorr levels and is signaled by a pronounced change in the emission spectra. Using $Eu_{0.9}Tb_{0.1}(tfa)_3(H_2O)_3$ as a case study, we showed that the intensity of the emission from Tb^{3+} becomes negligible in the low-pressure phase, while at the same time that of Eu^{3+} increases relative to the atmospheric phase. The low-pressure phase shows not only enhanced Tb-to-Eu energy transfer but also a multisite distribution of lanthanide ions over the semicrystalline lattice. The atmospheric-to-low-pressure transition is reversible and takes about a day to complete in either direction under the temperature and relative humidity conditions observed in this work. This transition is likely the result of disrupting low energy interactions such as

van der Waals and hydrogen bonds that are responsible for the long-range order observed in the atmospheric phase. Hydrogen bonds in particular are highly susceptible to partial or total dehydration occurring upon reducing pressure. From the standpoint of pressure and temperature sensing, pressure-dependent spectral changes observed in $Eu_{0.9}Tb_{0.1}(tfa)_3(H_2O)_3$ could be exploited to realize a two-state luminescent pressure sensor, though with the limitations imposed by the kinetics of the transition. On the other hand, the very weak intensity of the emission from Tb^{3+} relative to that of Eu^{3+} in the low-pressure phase limits the robustness of the red-to-green ratio as thermometric parameter in luminescence thermometry.

Open challenges encompass the fundamental aspects of the pressure-dependent transition as well as its potential for optical pressure sensing. Elucidating the atomic arrangement of the semicrystalline low-pressure phase and establishing the impact of relative humidity on the kinetics of the transition are of special interest. From a broader perspective, the observation of a pressure-dependent crystalline-to-semicrystalline transition in $Eu_{1-x}Tb_x(tfa)_3(H_2O)_3$ serves as a starting point to probe the implications of such a transition for the optical response of isostructural mixed-metal trifluoroacetates featuring other lanthanide pairs.

Conflicts of interest

There are no conflicts to declare.

Acknowledgements

The authors would like to acknowledge the financial support of the National Science Foundation (DMR 2003118), the Michigan Space Grant Consortium (Grant NNX15AJ20H), and the Department of Chemistry at Wayne State University. They also thank the Lumigen Instrument Center at Wayne State University for the use of the powder diffractometers (National Science Foundation MRI–1427926). Mr. Benjamin Oreskovic and Mr. Marcos Imer provided assistance to conduct variable-pressure luminescence experiments. Professor Leopoldo Suescun is acknowledged for helpful discussions.

Notes and references

1 J. E. Roberts, Lanthanum and Neodymium Salts of Trifluoroacetic Acid, *J. Am. Chem. Soc.*, 1961, **83**, 1087–1088.
2 J.-C. Boyer, F. Vetrone, L. A. Cuccia and J. A. Capobianco, Synthesis of Colloidal Upconverting NaYF4 Nanocrystals Doped with Er^{3+}, Yb^{3+} and Tm^{3+}, Yb^{3+} *via* Thermal Decomposition of Lanthanide Trifluoroacetate Precursors, *J. Am. Chem. Soc.*, 2006, **128**, 7444–7445.
3 X. Sun, Y.-W. Zhang, Y.-P. Du, Z.-G. Yan, R. Si, L.-P. You and C.-H. Yan, From Trifluoroacetate Complex Precursors to Monodisperse Rare-Earth Fluoride and Oxyfluoride Nanocrystals with Diverse Shapes through Controlled Fluorination in Solution Phase, *Chem. – Eur. J.*, 2007, **13**, 2320–2332.
4 Z. Quan, D. Yang, P. Yang, X. Zhang, H. Lian, X. Liu and J. Lin, Uniform Colloidal Alkaline Earth Metal Fluoride Nanocrystals: Nonhydrolytic Synthesis and Luminescence Properties, *Inorg. Chem.*, 2008, **47**, 9509–9517.
5 Y.-P. Du, Y.-W. Zhang, L.-D. Sun and C.-H. Yan, Optically Active Uniform Potassium and Lithium Rare Earth Fluoride Nanocrystals Derived from Metal Trifluoroacetate Precursors, *Dalton Trans.*, 2009, 8574–8581.
6 T. Paik, D.-K. Ko, T. R. Gordon, V. Doan-Nguyen and C. B. Murray, Studies of Liquid Crystalline Self-Assembly of GdF_3 Nanoplates by In-Plane, Out-of-Plane SAXS, *ACS Nano*, 2011, **5**, 8322–8330.
7 L. Yu, G. Li, Y. Liu, F. Jiang and M. Hong, Lanthanide-Doped KGd_2F_7 Nanocrystals: Controlled Synthesis, Optical Properties, and Spectroscopic Identification of the Optimum Core/Shell Architecture for Highly Enhanced Upconverting Luminescence, *Cryst. Growth Des.*, 2019, **19**, 2340–2349.
8 S. Fujihara, S. Koji, Y. Kadota and T. Kimura, Phase-Selective Pyrolysis and Pr^{3+} Luminescence in a YF_3–Y_2O_3 System from a Single-Source Precursor, *J. Am. Ceram. Soc.*, 2004, **87**, 1659–1662.
9 Y.-P. Du, Y.-W. Zhang, L.-D. Sun and C.-H. Yan, Luminescent Monodisperse Nanocrystals of Lanthanide Oxyfluorides Synthesized from Trifluoroacetate Precursors in High-Boiling Solvents, *J. Phys. Chem. C*, 2008, **112**, 405–415.
10 A. Gupta, R. Jagannathan, E. I. Cooper, E. A. Giess, J. I. Landman and B. W. Hussey, Superconducting Oxide-Films with High Transition Temperature Prepared from Trifluoroacetate Precursors onto (100) $SrTiO_3$, *Appl. Phys. Lett.*, 1988, **52**, 2077–2079.
11 P. C. McIntyre, M. J. Cima and M. F. Ng, Metal–Organic Deposition of High-J_c $YBa_2Cu_3O_{7-x}$ Thin Films from Trifluoroacetate Precursors onto (100) $SrTiO_3$, *J. Appl. Phys.*, 1990, **68**, 4183–4187.
12 T. Araki, K. Yamagiwa, I. Hirabayashi, K. Suzuki and S. Tanaka, Large-Area Uniform Ultrahigh J_c $YBa_2Cu_3O_{7-x}$ Film Fabricated by the Metalorganic Deposition Method using Trifluoroacetates, *Supercond. Sci. Technol.*, 2001, **14**, L21–L24.
13 A. Takeshi, Purified Coating Solution and Growth Scheme of the $YBa_2Cu_3O_{7-x}$ Superconductors in Metal Organic Deposition Using Trifluoroacetates, *Bull. Chem. Soc. Jpn.*, 2004, **77**, 1051–1061.
14 S. V. Larionov, V. N. Kirichenko, A. A. Rastorguev, V. I. Belyi, L. A. Sheludyakova, V. P. Fadeeva, V. M. Karpov, V. E. Platonov, N. I. Batrachenko and V. I. Lisoivan, Perfluorinated Europium(III) Carboxylates: Synthesis and Properties, *Russ. J. Coord. Chem.*, 1997, **23**, 432–438.
15 I. V. Kalinovskaya, V. V. Kon'shin, V. E. Karasev and E. N. Chernykh, Europium Complexes with Trifluoroacetic Acid, *Russ. J. Inorg. Chem.*, 1999, **44**, 380–383.
16 A. A. Rastorguev, A. A. Remova, G. V. Romanenko, N. P. Sokolova, V. I. Belyi and S. V. Larionov, Dimeric Structure and Electronic Conformation of $Tb(CF_3COO)_3{\cdot}3H_2O$ According to Luminescence Data, *J. Struct. Chem.*, 2001, **42**, 759–766.

17 V. I. Belyi, A. A. Rastorguev, A. A. Remova, G. V. Romanenko and N. P. Sokolova, Isomerism in the Terbium(III) Trifluoroacetate Trihydrate Dimer, *J. Struct. Chem.*, 2002, **43**, 587–594.
18 V. I. Belyi, A. A. Rastorguev, A. A. Remova, G. V. Romanenko and N. P. Sokolova, X-Ray Diffraction Analysis and Luminescent Study of the Structure of the $Tb_2(CF_3COO)_6(H_2O)_6$ Dimer Obtained from Terbium(III) Carbonate, *J. Struct. Chem.*, 2004, **45**, 130–138.
19 I. V. Kalinovskaya, A. N. Zadorozhnaya and Y. M. Nikolenko, Luminescent Properties of Europium Carboxylates, *J. Mol. Struct.*, 2015, **1100**, 100–104.
20 T. B. Emelina, I. V. Kalinovskaya and A. G. Mirochnik, Europium(III) Complex with Powerful Antenna Ligands: Interligand Interaction, *Spectrochim. Acta, Part A*, 2019, **207**, 222–228.
21 H. N. Munasinghe, R. G. Szlag, M. R. Imer and F. A. Rabuffetti, Synthesis, Structure, and Luminescence of Mixed-Ligand Lanthanide Trifluoroacetates, *Inorg. Chem.*, 2022, **61**, 5588–5594.
22 M. Ren, C. D. S. Brites, S.-S. Bao, R. A. S. Ferreira, L.-M. Zheng and L. D. Carlos, A Cryogenic Luminescent Ratiometric Thermometer Based on a Lanthanide Phosphonate Dimer, *J. Mater. Chem. C*, 2015, **3**, 8480–8484.
23 G. Bao, K.-L. Wong, D. Jin and P. A. Tanner, A Stoichiometric Terbium–Europium Dyad Molecular Thermometer: Energy Transfer Properties, *Light: Sci. Appl.*, 2018, **7**, 96.
24 A. N. Carneiro Neto, E. Mamontova, A. M. P. Botas, C. D. S. Brites, R. A. S. Ferreira, J. Rouquette, Y. Guari, J. Larionova, J. Long and L. D. Carlos, Rationalizing the Thermal Response of Dual−Center Molecular Thermometers: The Example of an Eu/Tb Coordination Complex, *Adv. Opt. Mater.*, 2022, **10**, 2101870.
25 A. M. Kaczmarek, Eu^{3+}/Tb^{3+} and Dy^{3+} POM@MOFs and 2D Coordination Polymers Based on Pyridine-2,6-Dicarboxylic Acid for Ratiometric Optical Temperature Sensing, *J. Mater. Chem. C*, 2018, **6**, 5916–5925.
26 J. K. Zaręba, M. Nyk, J. Janczak and M. Samoć, Three-Photon Absorption of Coordination Polymer Transforms UV-to-VIS Thermometry into NIR-to-VIS Thermometry, *ACS Appl. Mater. Interfaces*, 2019, **11**, 10435–10441.
27 Y. Cui, H. Xu, Y. Yue, Z. Guo, J. Yu, Z. Chen, J. Gao, Y. Yang, G. Qian and B. Chen, A Luminescent Mixed-Lanthanide Metal–Organic Framework Thermometer, *J. Am. Chem. Soc.*, 2012, **134**, 3979–3982.
28 X. Liu, S. Akerboom, M. D. Jong, I. Mutikainen, S. Tanase, A. Meijerink and E. Bouwman, Mixed-Lanthanoid Metal–Organic Framework for Ratiometric Cryogenic Temperature Sensing, *Inorg. Chem.*, 2015, **54**, 11323–11329.
29 I. N'Dala-Louika, D. Ananias, C. Latouche, R. Dessapt, L. D. Carlos and H. Serier-Brault, Ratiometric Mixed Eu–Tb Metal–Organic Framework as a New Cryogenic Luminescent Thermometer, *J. Mater. Chem. C*, 2017, **5**, 10933–10937.
30 M. Bettinelli and C. D. Flint, Non-Resonant Energy Transfer Between Tb^{3+} and Eu^{3+} in the Cubic Hexachloroelpasolite Crystals $Cs_2NaTb_{1-x}Eu_xCl_6$ (x = 0.01–0.15), *J. Phys.: Condens. Matter*, 1990, **2**, 8417–8426.
31 M. T. Berry, P. S. May and Q. Hu, Calculated and Observed Tb^{3+} ($^5D_4$) → Eu^{3+} Electronic Energy Transfer Rates in $Na_3[Tb_{0.01}Eu_{0.99}(oxydiacetate)_3]\cdot 2NaClO_4\cdot 6H_2O$, *J. Lumin.*, 1997, **71**, 269–283.
32 C. J. Kepert, L. Wei-Min, P. C. Junk, B. W. Skelton and A. H. White, Structural Systematics of Rare Earth Complexes. XI ('Maximally') Hydrated Rare Earth(III) Trifluoro- and Trichloro-acetates, *Aust. J. Chem.*, 1999, **52**, 459–480.
33 B. D. Dhanapala, H. N. Munasinghe, L. Suescun and F. A. Rabuffetti, Bimetallic Trifluoroacetates as Single-Source Precursors for Alkali–Manganese Fluoroperovskites, *Inorg. Chem.*, 2017, **56**, 13311–13320.
34 K. Liu, Y. Kang, Z. Wang and X. Zhang, 25th Anniversary Article: Reversible and Adaptive Functional Supramolecular Materials: "Noncovalent Interaction" Matters, *Adv. Mater.*, 2013, **25**, 5530–5548.
35 K. T. Dissanayake, L. M. Mendoza, P. D. Martin, L. Suescun and F. A. Rabuffetti, Open-Framework Structures of Anhydrous $Sr(CF_3COO)_2$ and $Ba(CF_3COO)_2$, *Inorg. Chem.*, 2016, **55**, 170–176.
36 B. D. Dhanapala, N. A. Mannino, L. M. Mendoza, K. Tauni Dissanayake, P. D. Martin, L. Suescun and F. A. Rabuffetti, Synthesis of Bimetallic Trifluoroacetates Through a Crystallochemical Investigation of Their Monometallic Counterparts: The Case of $(A, A')(CF_3COO)_2\cdot nH_2O$ (A, A′ = Mg, Ca, Sr, Ba, Mn), *Dalton Trans.*, 2017, **46**, 1420–1430.
37 H. Rietveld, Line Profiles of Neutron Powder-Diffraction Peaks for Structure Refinement, *Acta Crystallogr.*, 1967, **22**, 151–152.
38 H. Rietveld, A Profile Refinement Method for Nuclear and Magnetic Structures, *J. Appl. Crystallogr.*, 1969, **2**, 65–71.
39 A. C. Larson and R. B. Von Dreele, *General Structure Analysis System (GSAS)*, Los Alamos National Laboratory, 2000.
40 B. Toby, EXPGUI, a Graphical User Interface for GSAS, *J. Appl. Crystallogr.*, 2001, **34**, 210–213.
41 P. Thompson, D. E. Cox and J. B. Hastings, Rietveld Refinement of Debye–Scherrer Synchrotron X-ray Data from Al_2O_3, *J. Appl. Crystallogr.*, 1987, **20**, 79–83.
42 K. Momma and F. Izumi, VESTA 3 for Three-Dimensional Visualization of Crystal, Volumetric and Morphology Data, *J. Appl. Crystallogr.*, 2011, **44**, 1272–1276.
43 R. Shannon, Revised Effective Ionic Radii and Systematic Studies of Interatomic Distances in Halides and Chalcogenides, *Acta Crystallogr., Sect. A: Cryst. Phys., Diffr., Theor. Gen. Crystallogr.*, 1976, **32**, 751–767.
44 P. G. Wu and L. Brand, Resonance Energy Transfer: Methods and Applications, *Anal. Biochem.*, 1994, **218**, 1–13.
45 A. Sillen and Y. Engelborghs, The Correct Use of "Average" Fluorescence Parameters, *Photochem. Photobiol.*, 1998, **67**, 475–486.
46 G. Zatryb and M. M. Klak, On the Choice of Proper Average Lifetime Formula for an Ensemble of Emitters Showing Non-Single Exponential Photoluminescence Decay, *J. Phys.: Condens. Matter*, 2020, **32**, 415902.
47 R. A. Forman, G. J. Piermarini, J. D. Barnett and S. Block, Pressure Measurement Made by the Utilization of Ruby Sharp-Line Luminescence, *Science*, 1972, **176**, 284–285.

48 M. Back, J. Ueda, H. Hua and S. Tanabe, Predicting the Optical Pressure Sensitivity of $^2E \rightarrow {}^4A_2$ Spin-Flip Transition in Cr^{3+}-Doped Crystals, *Chem. Mater.*, 2021, **33**, 3379–3385.
49 Y. R. Shen, T. Gregorian and W. B. Holzapfel, Progress in Pressure Measurements with Luminescent Sensors, *High Press. Res.*, 1991, **7**, 73–75.
50 J. Rocha, C. D. S. Brites and L. D. Carlos, Lanthanide Organic Framework Luminescent Thermometers, *Chem. – Eur. J.*, 2016, **22**, 14782–14795.
51 Y. Chen, J. Qiu, Z. Chen, Y. Zhao, B. Li and C. Zeng, New Luminescent Lanthanide Complexes and Tb,Eu Co-Doped Complex as a Wide Temperature Self-Calibrating Thermometer, *Dyes Pigm.*, 2021, **194**, 109671.
52 L. Bellucci, G. Bottaro, L. Labella, F. Marchetti, S. Samaritani, D. Belli Dell'Amico and L. Armelao, 1D–Zigzag Eu^{3+}/Tb^{3+} Coordination Chains as Luminescent Ratiometric Thermometers Endowed with Multicolor Emission, *Materials*, 2021, **14**, 6445.
53 V. Trannoy, A. N. Carneiro Neto, C. D. S. Brites, L. D. Carlos and H. Serier-Brault, Engineering of Mixed Eu^{3+}/Tb^{3+} Metal–Organic Frameworks Luminescent Thermometers with Tunable Sensitivity, *Adv. Opt. Mater.*, 2021, **9**, 2001938.